ROYAL SOCIETY
OF CHEMISTRY

PAPER

Check for updates

Bandgap narrowing and piezochromism of doped two-dimensional hybrid perovskite nanocrystals under pressure†

Yue Shi,[a] Zongqing Jin,[a] Pengfei Lv,[a] Kai Wang, [ID][b] Guanjun Xiao [ID] *[a] and Bo Zou [ID][a]

Two-dimensional (2D) halide perovskites that incorporate organic interlayers show greatly improved environmental stability and optical tunability. Here, we provide a facile pressure engineering approach to achieve control over the optical features in Mn doped 2D perovskite $(PEA)_2PbBr_4$ (PEA^+ = $C_6H_5C_2H_4NH_3^+$) nanocrystals (NCs). Successive bandgap narrowing and marked piezochromism, which change the emission from orange to bluish violet, were realized. The bandgap of the Mn doped 2D perovskite $(PEA)_2PbBr_4$ NCs was steadily reduced by 480 meV under high pressure, which is much larger than that of conventional Mn-doped three-dimensional (3D) perovskite $CsPbBr_3$ NCs (with a bandgap tuning of about 100 meV). In addition, the intrinsic band edge emission of Mn doped 2D perovskite $(PEA)_2PbBr_4$ NCs was stabilized up to 9.2 GPa. The unique steric and spring effects of asymmetric organic PEA^+ bilayers accommodated the slow octahedral deformation under pressure. Furthermore, the doping of elemental Mn greatly facilitated the local lattice distortion of the 2D perovskite $(PEA)_2PbBr_4$ NCs under high pressure, which was attributed to the appearance of enhanced self-trapped exciton (STE) emission. Our studies elucidated the structure–property relationship of Mn doped layered $(PEA)_2PbBr_4$ NCs, thus providing a basis for their applications in opto-pressure sensing.

Introduction

Two-dimensional (2D) hybrid perovskites are promising candidates for optoelectronic applications because of their unique electronic properties.[1–7] They differ significantly from traditional three-dimensional (3D) perovskites owing to their layered structures which give them structural diversity since the 2D counterparts are susceptible to external driving forces. Furthermore, doping other ions into perovskites can form an impurity energy level in the bandgap. Through energy transfer between two different excited states, dual emission exhibits visually distinguishable luminescence that enriches the optical properties of the perovskites.[8,9] The doping of 2D perovskites can further improve their photoluminescence quantum yield (PLQY) values, and achieve a wide color gamut display.[10–14] As a typical example, Mn^{2+} doping in 2D perovskites has been

achieved using a simple direct synthesis method, leading to perovskites with the characteristic Mn^{2+} dual-emission.[15,16]

High pressure, one of the benign extreme conditions, has created a number of novel phenomena that fail to materialize under ambient conditions.[17–21] The loading of pressure using a diamond anvil cell (DAC) acting on matter has been able to successfully fabricate new materials, discover exotic phenomena or solve scientific disputes. Using pressure, Lv *et al.* achieved a near 100% PLQY in one-dimensional (1D) hybrid metal halides, and unraveled the underlying mechanisms of pressure gating.[22,23] Moreover, through changing the structure with pressure, Zou *et al.* promoted a non-luminescent material to exhibit emission and retained the strong emission under ambient conditions, as well as reducing the bandgap to achieve perovskite metallization, *etc.*[24–29] Doping Mn^{2+} combined with pressure will shorten the distance between molecules and amplify deformation of the octahedral framework, thus directly enhancing the photoelectric characteristics.[30,31]

Herein, we provide a facile pressure engineering approach to investigate the pressure response of optical properties and structural alterations for Mn^{2+} doped 2D perovskite $(PEA)_2PbBr_4$ (PEA^+ = $C_6H_5C_2H_4NH_3^+$) nanocrystals (NCs). We were able to accomplish a significant narrowing of the bandgap as well as a piezochromic phenomenon with a marked

[a] *State Key Laboratory of Superhard Materials, College of Physics, Jilin University, Changchun, 130012, P. R. China. E-mail: xguanjun@jlu.edu.cn*

[b] *Shandong Key Laboratory of Optical Communication Science and Technology, School of Physics Science and Information Technology, Liaocheng University, Liaocheng, 252000, China*

† Electronic supplementary information (ESI) available. See DOI: https://doi.org/10.1039/d2tc05158c

modulation of the PL emission from orange to blue-violet. The bandgap narrowing reached 480 meV, and the band edge emission was gradually red-shifted to remain stable up to 9.2 GPa. The changes were strongly related to the unique steric and spring effect of the asymmetric organic PEA$^+$ cation bilayers. In addition, the emission of STEs was produced through the 2D structure's quantum confinement effect, as well as the local lattice distortion caused by the doped Mn^{2+} under high pressure. Our studies provide insight for the design of materials with potential applications in opto-pressure sensing.

Results and discussion

The modulation of the bandgap was directly related to the band edge emission shifts under pressure. As a result, high-pressure optical absorption was used to delve deeper into the quantitative data on pressure-dependent band-edge emission changes. Under ambient conditions, the absorption edge of Mn-doped (PEA)$_2$PbBr$_4$ NCs was approximately 410.5 nm, which coincided perfectly with the band edge emission (Fig. S1, ESI†).[11] Upon compression, the absorption edge exhibited a gradual red shift, accompanied by a sustainable bandgap narrowing of ~480 meV until 9.2 GPa (Fig. 1a). Beyond 9.2 GPa, the disappearance of the absorption edge of the Mn doped (PEA)$_2$PbBr$_4$ NCs suggested the disappearance of the exciton absorption peak, accompanied by a blue shift (Fig. S3, ESI†). Using the extrapolated linear portion of the $(\alpha h\nu)^2$ versus $h\nu$ curve, the bandgap of the material was estimated (inset in Fig. 1b and Fig. S2, ESI†), where α is the absorption coefficient, and $h\nu$ is the photon energy. At the same time, the band edge emission also showed a pressure-dependent red-shift and was detectable up to 9.2 GPa. Comparative changes in the absorption and PL spectra of the Mn-doped (PEA)$_2$PbBr$_4$ NCs under pressure are shown in Fig. 1c. The normalized band edge emission, as illustrated in Fig. 1d, demonstrated a wide range of stability and a red shift of approximately 63.8 nm. All of this resulted from the unique steric hindrance structure of the asymmetric organic PEA$^+$ cation bilayers, which enabled the existence of two separate compression regimes dominated by softer organic and rigid inorganic layers.[32,33] When the pressure was completely released, the absorption spectra demonstrated reversibility under pressure (Fig. S4, ESI†).

The Mn-doped (PEA)$_2$PbBr$_4$ NCs exhibited a dual emission which incorporated the band edge emission (410.5 nm) and a Mn-related emission (611.6 nm) under ambient conditions. The new dynamic equilibrium changed the energy transfer between the two excited states when the sample was subjected to external pressure. To reveal the pressure response of optical properties of the Mn-doped (PEA)$_2$PbBr$_4$ NCs, we performed *in situ* high-pressure PL measurements at room temperature. Fig. 2a and b and Fig. S5 (ESI†) show that the two emissions all underwent considerable linear redshifts as the pressure was increased; the band edge emission redshifted from 410.5 nm to 452.9 nm (4.4 GPa), while the Mn-related emission redshifted from 611.3 nm to 663.3 nm (4.4 GPa) (Fig. S6a, ESI†). In particular, the band edge emission was more stable up to
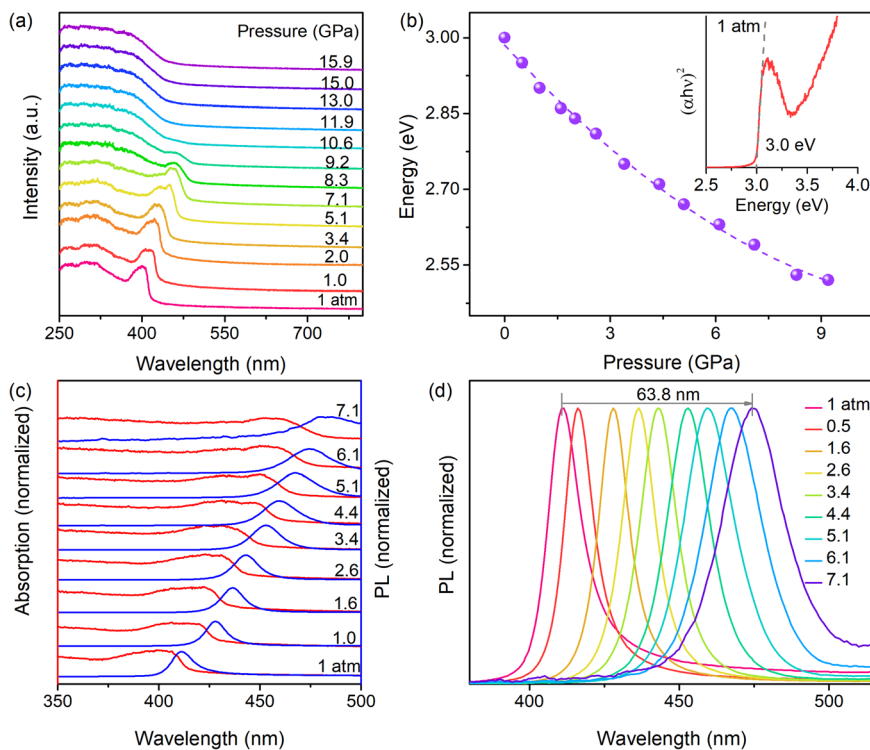

Fig. 1 (a) Absorption spectra of Mn–doped (PEA)$_2$PbBr$_4$ NCs as a function of pressure. (b) Pressure-dependent bandgap evolution of Mn–doped (PEA)$_2$PbBr$_4$ NCs as a function of pressure. The inset shows the Tauc plot for Mn–doped (PEA)$_2$PbBr$_4$ NCs under ambient conditions. (c) Changes in the absorption and PL spectra of Mn–doped (PEA)$_2$PbBr$_4$ NCs under pressure. (d) Band edge emission of Mn–doped (PEA)$_2$PbBr$_4$ NCs under high pressure.

This journal is © The Royal Society of Chemistry 2023

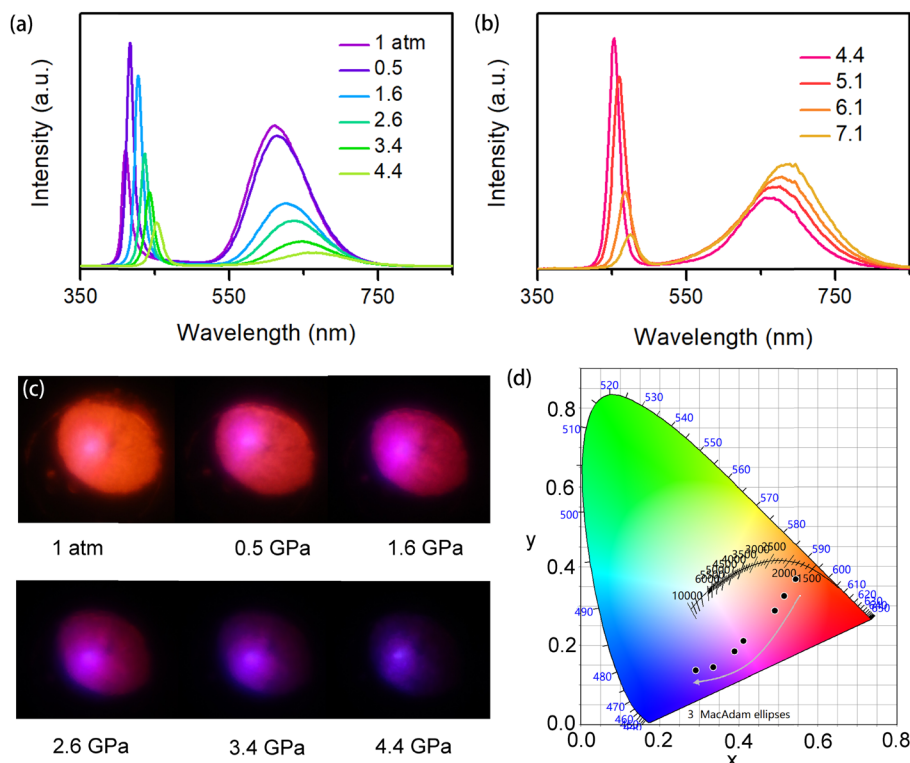*J. Mater. Chem. C*, 2023, **11**, 1726–1732 | **1727**

Fig. 2 (a and b) PL spectra of Mn-doped $(PEA)_2PbBr_4$ NCs under high pressure. (c) PL micrographs upon compression. (d) Pressure-dependent chromaticity coordinates of the emissions.

9.2 GPa and exhibited a bigger red shift under pressure compared with either Mn-doped 3D $CsPbBr_3$ or $CsPbCl_3$ NCs.[30,31] This is attributed to the steric and spring effect of the large organic cations (PEA^+), which have a certain buffering effect on the structure under pressure.

Note that as the pressure continued to rise from 4.4 GPa, there was a weak enhancement in the low-energy fluorescence with pressure to 7.1 GPa. It makes sense to relate this to an increase in the emission of STEs, which was observed in pristine $(PEA)_2PbBr_4$ under pressure as an increase in the STE emission peak and a decrease in the band edge emission (4.0 GPa).[33] In addition, the local lattice deformation brought on by Mn^{2+} doping and the large exciton binding energy of the 2D layered structure were significant factors in the generation and enhancement of the emission of STEs under pressure. Throughout the compression process, piezochromism was achieved with the continuous red shift and alternating strength of the dual emission peaks. The matching PL photographs taken under UV-irradiation are depicted in Fig. 2c and Fig. S7 (ESI†), which can be seen intuitively in the colour changes from orange to bluish violet. In addition, the CIE chromaticity coordinates of Mn-doped $(PEA)_2PbBr_4$ could be controlled from orange to bluish violet *via* control of the pressure (Fig. 2d). Furthermore, in comparing the PL emission spectra a weakening in intensity was seen (Fig. S8, ESI†), which could be related to the deviatoric stress across the samples under higher pressures.[34,35] Deviatoric stress usually leads to large aggregation and breaking in the recovered samples, which decreases

the crystallinity and increases defects and surface-related exciton trap states.[36,37]

So as to clarify the relationship between the optical properties and the structure of the Mn-doped $(PEA)_2PbBr_4$ NCs, *in situ* high-pressure ADXRD experiments were conducted. Fig. 3a shows the ADXRD patterns of the Mn-doped $(PEA)_2PbBr_4$ NCs at pressures up to 20.6 GPa. With increasing pressure, all peaks shifted to higher diffraction angles, indicating a contraction of the volume. In addition, there were not many changes following compression other than a slow, amorphous process indicated by the widening of the diffraction peaks. To obtain more structural information, the changes in the lattice constants and volume of the Mn-doped $(PEA)_2PbBr_4$ NCs were studied *via* structural refinement upon compression (Fig. 3b and c). The lattice of the *a*-axis was easily compressed due to the complexly configurational organic molecules [PEA^+]. The lattice constants of the *a*-axis decreased by 0.6058 Å with pressure up to 9.1 GPa, while those of the *b*- and *c*-axes decreased by 0.2548 Å and 0.5222 Å, correspondingly (as shown in Table S1, ESI†). We further fitted the experimental pressure–volume data of the Mn-doped $(PEA)_2PbBr_4$ NCs by utilizing the third-order Birch–Murnaghan equation of state as follows:

$$P(v) = \frac{3B_0}{2}\left[\left(\frac{V_0}{V}\right)^{7/3} - \left(\frac{V_0}{V}\right)^{5/3}\right]\left\{1 + \frac{3}{4}(B_0' - 4)\left[\left(\frac{V_0}{V}\right)^{2/3} - 1\right]\right\}$$

where V_0 is the zero-pressure volume, B_0 is the bulk modulus at ambient pressure, and B_0' is a parameter for the pressure
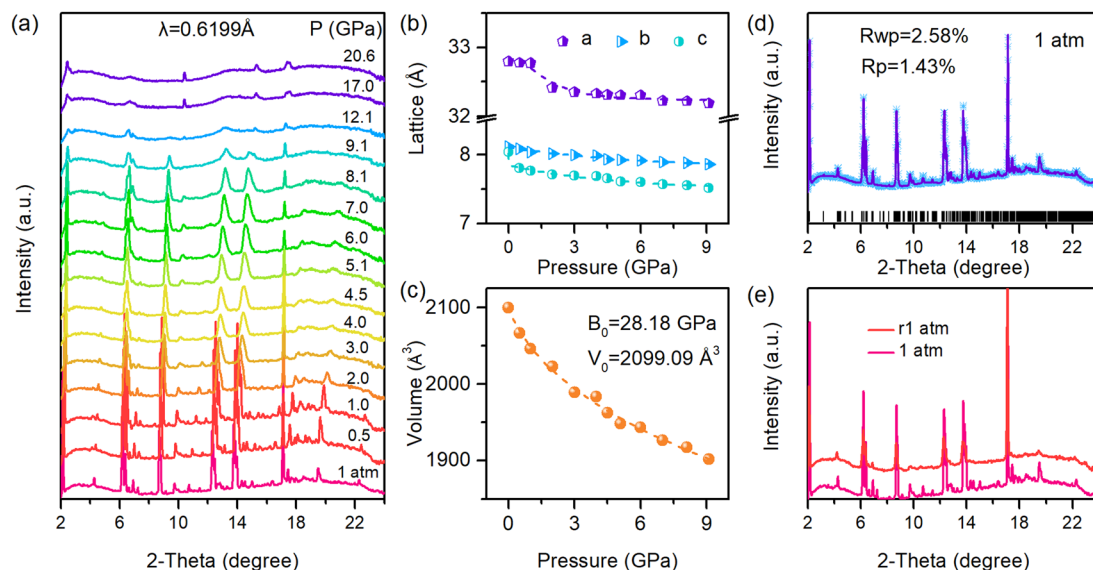
1728 | *J. Mater. Chem. C*, 2023, **11**, 1726–1732

This journal is © The Royal Society of Chemistry 2023

Fig. 3 (a) Selected high-pressure ADXRD patterns for Mn-doped $(PEA)_2PbBr_4$ NCs. (b) Pressure dependence of lattice constants for Mn-doped $(PEA)_2PbBr_4$ NCs. (c) Cell volume evolution of Mn-doped $(PEA)_2PbBr_4$ NCs upon compression. (d) Rietveld refinement results for the Mn-doped $(PEA)_2PbBr_4$ NCs at 1 atm. (e) Contrasted ADXRD patterns between ambient conditions (1 atm) and after decompression (r1 atm).

derivative. Rietveld refinement of the ADXRD patterns of the Mn-doped $(PEA)_2PbBr_4$ NCs under ambient conditions is shown in Fig. 3d. The ambient-conditions ADXRD data were fitted to the orthorhombic system ($a = 32.7948$ Å, $b = 8.1174$ Å, $c = 8.0359$ Å), matching well with the experimental data ($R_p = 2.58\%$, $R_{wp} = 1.43\%$). When the pressure was completely released, the structure exhibited the reversibility of the pressure-driven amorphous process (Fig. 3e). Moreover, contrasting the absorption spectra obtained under ambient conditions and after decompression also indicated the structure reversibility.

We quantitatively evaluated the structural compression process to better understand the pressure-induced structure changes. The 2D layered crystal structure along the crystallographic a-axis displayed asymmetric organic PEA^+ cation bilayers alternating with inorganic layers, generating a "sandwich" structure from different axis viewpoints, as shown in Fig. 4a and the inset in Fig. 4b. Corner-sharing $PbBr_6$ and $MnBr_6$ octahedra were used to create the single inorganic layer within the bc-plane. The 2D interlayer structure should compress more readily and exhibit a higher compressibility. As the pressure was increased gradually, the structure became more compact, which causes the compressibility to progressively decline. It is clear from Fig. 4b that the a-axis compressed more quickly up to 1.0 GPa, which serves as a buffer layer
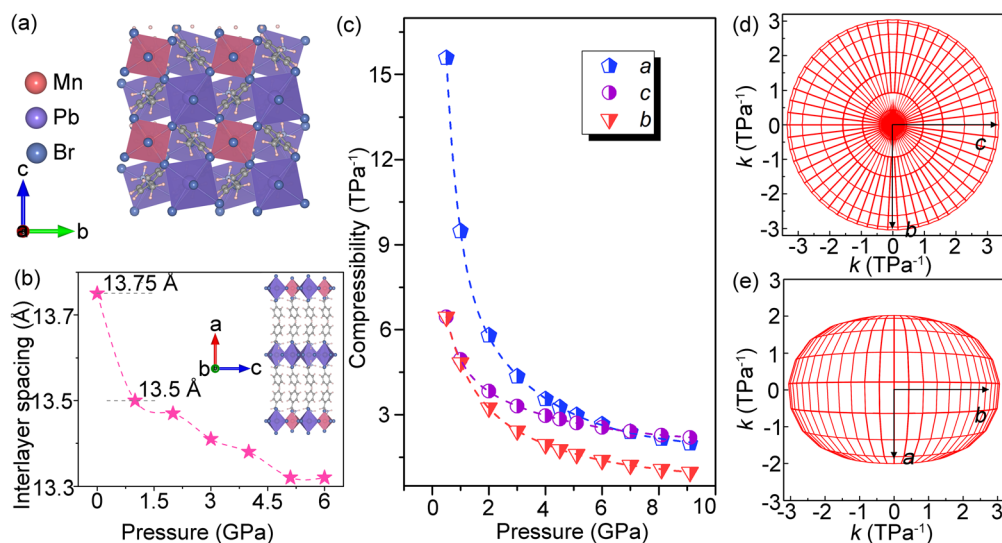

Fig. 4 (a) Crystal structure along the a axis. (b) Change in interlayer spacing as a function of pressure. (c) Compressibility of the lattice axes in Mn-doped $(PEA)_2PbBr_4$ NCs. (d and e) Compressibility indicatrix in the bc and ab planes of Mn-doped $(PEA)_2PbBr_4$ NCs.
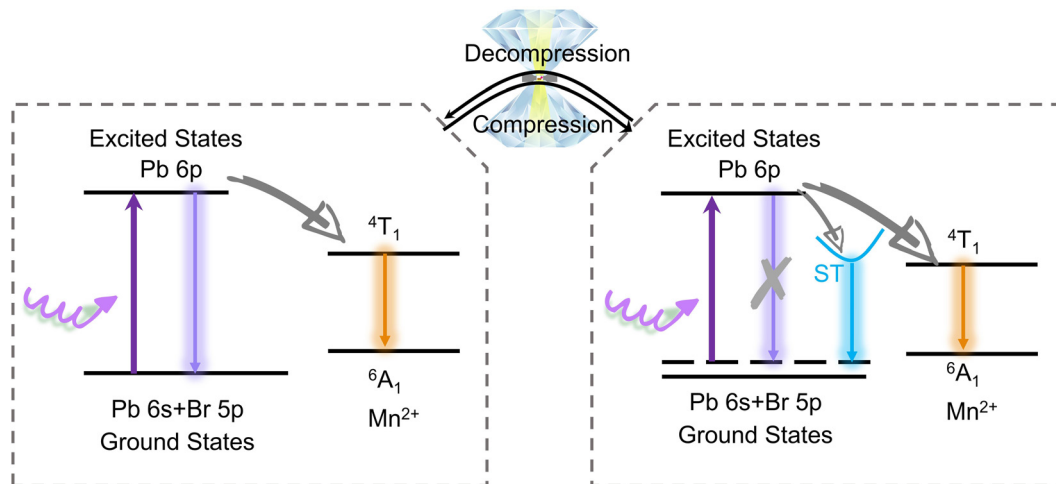
Fig. 5 Configuration coordinate models for Mn doped $(PEA)_2PbBr_4$ under ambient conditions and high pressure. Therein, ST denotes self-trapped states.

during the crystal compression process. The spacing of the PEA^+ cations with large molecules was reduced from 13.75 to 13.5 Å up to 1.0 GPa for the interlayer structures (Fig. 4c). The reduction tends to slow down upon further compression.

Meanwhile, to explore all the three directional structural responses of the layered crystal structure, the high-pressure compressibility was calculated, as shown in Fig. 4d and e. The interlayer direction of the a-axis has a higher compressibility (K_a) than the inorganic intra-layer direction of the b- and c-axes (K_b and K_c, respectively). The change in trend of the layer structure under pressure can also be more intuitively revealed through a qualitative study of the structure. We further explored the distortion of different Mn–Br and Pb–Br octahedra within Mn-doped $(PEA)_2PbBr_4$ NCs under pressure, as shown in the Fig. S9 and S10 (ESI†). Under pressure, the distortion in the bond length values (Δd) of the $PbBr_6$ and $MnBr_6$ octahedra in the structure was almost the same, but the variance in the octahedral angle (δ^2 values) changes. When the pressure was increased to 4.0 GPa, more distortion was generated to render much stronger electron–phonon coupling. Because of this, the activation energy of de-trapping was enhanced, thus stabilizing more STEs.

Pristine $(PEA)_2PbBr_4$ exhibited a sharp and narrow blue band edge emission centered at ~416 nm, which decreases continuously under pressure.[33] However, Mn^{2+} doped $(PEA)_2PbBr_4$ NCs introduced a new emission channel at ~610 nm owing to an internal $^4T_1$-to-$^6A_1$ transition of the Mn ion (left in Fig. 5).[38] Upon compression, due to the unique steric and spring effects of the asymmetric organic PEA^+ cation bilayers, the pressure points of bandgap narrowing and piezochromism were hysteretic, compared with traditional Mn^{2+} doped 3D perovskite $CsPbBr_3$. The valence band maximum (VBM) energy would be increased because of the enhanced coupling between the Pb 6s and the Br 4p orbitals. By contrast, the conduction band minimum (CBM) was mainly determined by the non-bonding localized state of Pb 6p orbitals that are insensitive to pressure. Accordingly, a persistently decreased bandgap was observed under high pressure. In the low-pressure range, the interlayer spacing of the soft organic cation layer was first compressed, which reduces the impact of the pressure on the inorganic octahedral layer and causes a slow redshift of the bandgap.[32,39] With a further increase in the pressure, the competition between the interlayer contraction and lattice distortion gives rise to moderate band-gap narrowing.

Furthermore, the strong exciton–phonon coupling in a deformed lattice will lead to localization of the carriers. This facilitated the formation of stable STEs and corresponding STE emission. In addition, different from pristine $(PEA)_2PbBr_4$, the smaller radius of the dopant Mn^{2+} compared with Pb^{2+} resulted in the large distortion of the lattice. Meanwhile the pressure will enlarge distortion significantly until an amorphous state is reached. The highly distorted structure and the strong exciton–phonon coupling eventually lead to the formation of trapped excitons and thus radiative recombination.[22] Likewise, the structure subsequently becomes unstable with the increase in pressure, which in turn causes weakening of the STE emission.

Conclusions

In summary, *via* the application of pressure to Mn doped 2D perovskite $(PEA)_2PbBr_4$, we achieved successive bandgap narrowing and marked piezochromism, which changes the emission from orange to bluish violet. The bandgap steadily contracted by 480 meV, and the band edge emission was stabilized up to a pressure of 9.2 GPa. Because of the 2D layered structure with the unique steric and spring effects of the asymmetric organic cation bilayers, the optical properties of the Mn doped $(PEA)_2PbBr_4$ NCs differed greatly different from those of the Mn doped 3D $CsPbBr_3$ NCs. Furthermore, the emission of STEs was produced under pressure as a result of the increased local lattice deformation upon Mn^{2+} doping during pressurization. Our studies unraveled the structure–property relationship in 2D perovskite $(PEA)_2PbBr_4$, which

could provide potential applications in opto-pressure sensing and optoelectronic devices.

Conflicts of interest

There are no conflicts to declare.

Acknowledgements

Notes and references

1 L. T. Dou, A. B. Wong, Y. Yu, M. L. Lai, N. Kornienko, S. W. Eaton, A. Fu, C. G. Bischak, J. Ma, T. Ding, N. S. Ginsberg, L. W. Wang, A. P. Alivisatos and P. D. Yang, *Science*, 2015, **349**, 1518–1521.

2 J. C. Blancon, J. Even, C. C. Stoumpos, M. G. Kanatzidis and A. D. Mohite, *Nat. Nanotechnol.*, 2020, **15**, 969–985.

3 F. Zhang, H. Lu, J. Tong, J. J. Berry, M. C. Beard and K. Zhu, *Energy Environ. Sci.*, 2020, **13**, 1154–1186.

4 E. S. Vasileiadou, B. Wang, I. Spanopoulos, I. Hadar, A. Navrotsky and M. G. Kanatzidis, *J. Am. Chem. Soc.*, 2021, **143**, 2523–2536.

5 W. Tao, Y. Zhang and H. Zhu, *Acc. Chem. Res.*, 2022, **55**, 345–353.

6 G. Mohanty, A. Sebastian, S. Haritha, K. N. Parida and I. Neogi, *J. Mater. Chem. C*, 2022, **10**, 16949–16982.

7 X. Liu, M. Tai, J. Gu, Z. Wu, H. Zhong, X. Wang, Z. Wang and H. Lin, *J. Mater. Chem. C*, 2022, **10**, 10964–10972.

8 Y. Liu, M. L. Zaffalon, J. Zito, F. Cova, F. Moro, M. Fanciulli, D. X. Zhu, S. Toso, Z. G. Xia, I. Infante, L. D. Trizio, S. Brovelli and L. Manna, *Chem. Mater.*, 2022, **34**, 8603–8612.

9 C. Li, Z. Luo, Y. Liu, Y. Wei, X. He, Z. Chen, L. Zhang, Y. Chen, W. Wang, Y. Liu, X. Chang and Z. Quan, *Adv. Opt. Mater.*, 2022, **10**, 2102746.

10 S. Sarang, W. Delmas, S. Bonabi Naghadeh, V. Cherrette, J. Z. Zhang and S. Ghosh, *J. Phys. Chem. Lett.*, 2020, **11**, 10368–10374.

11 X. Gao, X. Shen, D. Xue, X. Li, P. Lu, M. Lu, C. Li, W. W. Yu and X. Bai, *Mater. Chem. Front.*, 2021, **5**, 937–943.

12 J. Zhou, S. Guo, J. Zhao, M. Molokeev, Q. Liu, J. Zhang and Z. Xia, *Sci. China Mater.*, 2019, **62**, 1013–1022.

13 H. Zhang, J. Yao and H. Fu, *Adv. Opt. Mater.*, 2020, **9**, 2001135.

14 S. Wang, D. Wu, S. Yang, H. Zhen, Z. Lin and Q. Ling, *J. Mater. Chem. C*, 2020, **8**, 12623–12631.

15 H. Zhang, J. Yao, K. Zhou, Y. Yang and H. Fu, *Chem. Mater.*, 2022, **34**, 1854–1861.

16 C. Sun, Z. Gao, Y. Deng, H. Liu, L. Wang, S. Su, P. Li, H. Li, Z. Zhang and W. Bi, *ACS Appl. Mater. Interfaces*, 2019, **11**, 34109–34116.

17 Z. Ma, Q. Li, J. Luo, S. Li, L. Sui, D. Zhao, K. Yuan, G. Xiao, J. Tang, Z. Quan and B. Zou, *J. Am. Chem. Soc.*, 2021, **143**, 15176–15184.

18 Y. Fang, L. Zhang, Y. Yu, X. Yang, K. Wang and B. Zou, *CCS Chem.*, 2021, **3**, 2203–2210.

19 Z. Ma, F. Li, D. Zhao, G. Xiao and B. Zou, *CCS Chem.*, 2020, **2**, 71–80.

20 L. Meng, J. M. D. Lane, L. Baca, J. Tafoya, T. Ao, B. Stoltzfus, M. Knudson, D. Morgan, K. Austin, C. Park, P. Chow, Y. Xiao, R. Li, Y. Qin and H. Fan, *J. Am. Chem. Soc.*, 2020, **142**, 6505–6510.

21 Q. Li, Z. Chen, M. Li, B. Xu, J. Han, Z. Luo, L. Tan, Z. Xia and Z. Quan, *Angew. Chem., Int. Ed.*, 2021, **60**, 2583–2587.

22 H. Luo, S. Guo, Y. Zhang, K. Bu, H. Lin, Y. Wang, Y. Yin, D. Zhang, S. Jin, W. Zhang, W. Yang, B. Ma and X. Lv, *Adv. Sci.*, 2021, **8**, 2100786.

23 S. Guo, Y. Li, Y. Mao, W. Tao, K. Bu, T. Fu, C. Zhao, H. Luo, Q. Hu, H. Zhu, E. Shi, W. Yang, L. Dou and X. Lv, *Sci. Adv.*, 2022, **8**, eadd1984.

24 Z. Ma, Z. Liu, S. Lu, L. Wang, X. Feng, D. Yang, K. Wang, G. Xiao, L. Zhang, S. A. T. Redfern and B. Zou, *Nat. Commun.*, 2018, **9**, 4506.

25 Y. Shi, Z. Ma, D. Zhao, Y. Chen, Y. Cao, K. Wang, G. Xiao and B. Zou, *J. Am. Chem. Soc.*, 2019, **141**, 6504–6508.

26 Y. Fang, L. Zhang, L. Wu, J. Yan, Y. Lin, K. Wang, W. L. Mao and B. Zou, *Angew. Chem., Int. Ed.*, 2019, **58**, 15249–15253.

27 R. Fu, W. Zhao, L. Wang, Z. Ma, G. Xiao and B. Zou, *Angew. Chem., Int. Ed.*, 2021, **60**, 10082–10088.

28 D. Zhao, G. Xiao, Z. Liu, L. Sui, K. Yuan, Z. Ma and B. Zou, *Adv. Mater.*, 2021, **33**, 2100323.

29 L. Zhang, C. Liu, L. Wang, C. Liu, K. Wang and B. Zou, *Angew. Chem., Int. Ed.*, 2018, **57**, 11213–11217.

30 Y. Cao, G. Qi, L. Sui, Y. Shi, T. Geng, D. Zhao, K. Wang, K. Yuan, G. Wu, G. Xiao, S. Lu and B. Zou, *ACS Mater. Lett.*, 2020, **2**, 381–388.

31 Y. Shi, W. Zhao, Z. Ma, G. Xiao and B. Zou, *Chem. Sci.*, 2021, **12**, 14711–14717.

32 G. Liu, L. Kong, P. Guo, C. C. Stoumpos, Q. Hu, Z. Liu, Z. Cai, D. J. Gosztola, H.-K. Mao, M. G. Kanatzidis and R. D. Schaller, *ACS Energy Lett.*, 2017, **2**, 2518–2524.

33 L. Zhang, L. Wu, K. Wang and B. Zou, *Adv. Sci.*, 2019, **6**, 1801628.

34 Y. Nagaoka, K. Hills-Kimball, R. Tan, R. Li, Z. Wang and O. Chen, *Adv. Mater.*, 2017, **29**, 1606666.

35 H. Zhu, T. Cai, M. Que, J. P. Song, B. M. Rubenstein, Z. Wang and O. Chen, *J. Phys. Chem. Lett.*, 2018, **9**, 4199–4205.

36 J. S. Manser, M. I. Saidaminov, J. A. Christians, O. M. Bakr and P. V. Kamat, *Acc. Chem. Res.*, 2016, **49**, 330–338.

This journal is © The Royal Society of Chemistry 2023

J. Mater. Chem. C, 2023, **11**, 1726–1732 | 1731

37 Z. Ma, F. Li, G. Qi, L. Wang, C. Liu, K. Wang, G. Xiao and B. Zou, *Nanoscale*, 2019, **11**, 820–825.

38 W. Liu, Q. Lin, H. Li, K. Wu, I. Robel, J. M. Pietryga and V. I. Klimov, *J. Am. Chem. Soc.*, 2016, **138**, 14954–14961.

39 J. Lin, H. Chen, Y. Gao, Y. Cai, J. Jin, A. S. Etman, J. Kang, T. Lei, Z. Lin, M. C. Folgueras, L. N. Quan, Q. Kong, M. Sherburne, M. Asta, J. Sun, M. F. Toney, J. Wu and P. Yang, *Proc. Natl. Acad. Sci. U. S. A.*, 2019, **116**, 23404–23409.

1732 | *J. Mater. Chem. C*, 2023, **11**, 1726–1732

This journal is © The Royal Society of Chemistry 2023